Quantifying the Termination Mechanism Along the North Tabriz-North Mishu Fault Zone of Northwestern Iran via Small Baseline PS-InSAR and GPS Decomposition

Zhe Su, Er-Chie Wang, Jyr-Ching Hu, Morteza Talebian, and Sadra Karimzadeh

***Abstract*—Quantitative understanding of stress transfer between major fault systems can elucidate the kinematics of large-scale plate interactions. This study analyzed right-lateral strike-slip motion on the North Tabriz fault (NTF) in an area where this structure appears to transition into a thrust fault known as the North Mishu fault (NMF). These faults play an important but cryptic role in accommodating stress related to the Arabia-Eurasia plate collision. We analyzed regional velocity vectors from permanent and temporary GPS arrays to estimate changes in fault-parallel and fault-normal slip rates in the transition zone between the NTF and NMF. Independent of its compressional motion, the NMF exhibits a dextral strike-slip rate of ∼2.62 mm/yr. Along the NTF, the right-lateral slip rate decreases and the vertical slip rate on increases at rates of 0.08 and 0.38 mm/yr km, respectively, as the NTF approaches the NMF. This study also used small baseline (SBAS) PS-InSAR results to reveal a NE-SW-striking reverse fault and a developing syncline hidden beneath the Tabriz Basin. Additionally, we calculated the vertical displacement rates using horizontal vectors from the GPS data and mean line-of-sight rate estimates from the SBAS data. While the study area does not express large-scale extrusion, such as that observed in the Anatolian Plate, the transformation of strike-slip motion into thrusting and crustal shortening along the NMF-NTF fault zone accommodates most of the N–S compression affecting the northwestern Iranian Plateau. In this region, small-sized, right-lateral strike-slip faults, and other folded structures form horsetail features. These dispersed structures accommodate eastward extrusion of the northwestern Iranian Plateau.**

***Index Terms*—GPS velocity decomposition, northwestern Iranian Plateau, small baseline PS-InSAR, stress transfer at fault terminations.**

Manuscript received November 18, 2015; revised March 3, 2016 and May 4, 2016; accepted June 14, 2016. Date of publication September 7, 2016; date of current version December 22, 2016. This work was supported by the National Natural Science Foundation of China for Youth under Grant 41502219, Cross Strait Cooperation Project Grant 4141101073, the Self-Determined Project under Grant 11511270 from the State Key Laboratory of Lithospheric Evolution, Institute of Geology and Geophysics, Chinese Academy of Sciences, the "Strategic Priority Research Program" of Chinese Academy of Sciences under Grants XDB03010800 and XDB03010500, and the Silk Road Project (II): Tibet/Himalaya versus Caucasus/Iran Orogenic Belts form Excellent Research Projects of National Taiwan University under Grant 101-105R891204. *(Corresponding author: Zhe Su.)*

Z. Su was with the State Key Laboratory of Lithospheric Evolution, Institute of Geology and Geophysics, Chinese Academy of Sciences, Beijing 100029, China and also with the Department of Geosciences, National Taiwan University, Taipei 10617, Taiwan. He is now with the Key Laboratory of Crustal Dynamics, Institute of Crustal Dynamics, China Earthquake Administration, Beijing, China (e-mail: szhe1230@126.com).

E.-C. Wang is with the State Key Laboratory of Lithospheric Evolution, Institute of Geology and Geophysics, Chinese Academy of Sciences, Beijing 100101, China (e-mail: erchie-wang@mail.iggcas.ac.cn).

J.-C. Hu is with the Department of Geosciences, National Taiwan University, Taipei 10617 (e-mail: jchu@ntu.edu.tw).

M. Talebian is with the Research Institute for Earth Science, Geological Survey of Iran, Tehran 1996715433, Iran (e-mail: morteza100@yahoo.com).

S. Karimzadeh is with the Faculty of Environmental Design, Kanazawa University, Kanazawa 920-1192, Japan, and also with the Department of GIS and Remote Sensing, University of Tabriz, Tabriz 51666-14766, Iran (e-mail: sadra.karimzadeh@gmail.com).

Color versions of one or more of the figures in this paper are available online at http://ieeexplore.ieee.org.

Digital Object Identifier 10.1109/JSTARS.2016.2586742

I. Introduction

A LARGE-SCALE fault at an active plate boundary cannot simply disappear. Nearby structures should represent adequate structural mechanisms for absorbing the stress/strain [1]–[3]. The large-scale strike-slip faults within and around the Tibetan Plateau, for example, accommodate and transfer a degree of stress that is generally consistent with the overall estimates of the local expression of the India-Eurasia plate collision. The Altyn Tagh fault is a 2000-km-long lineation bounding the northern margin of the Tibetan Plateau. Its left-lateral strike-slip motion accommodates the northward and/or northeastward growth of the Tibetan Plateau. At its western terminus, the sinistral shear of the Altyn Tagh fault transitions into uplift of the western Kunlun Mountains [4], [5], while vertical overthrusting of the Qilian Shan (e.g., [6]) occurs at its eastern terminus. The highest mountain along the southeast margin of the Tibetan Plateau, Mount Gongga (7566 m), provides an additional example of stress transfer. Wang *et al.* [7] attribute uplift of this feature to transfer of left-lateral strike-slip along the Xianshuihe fault at its southern terminus. The above examples represent qualitative or semiquantitative interpretations. Additional quantitative analysis can help us to inform our understanding of stress transfer along major faults in active collision zones.

The Turkish-Iranian Plateau formed due to the approximately northward movement of the Arabian plate with respect to the Eurasian plate. The plateau exhibits active faulting, fold development above blind thrusts, volcanic activity [8], and considerable topographic relief typical of the overall Alpine-Himalayan mountain belts (e.g., [9]). The Anatolian Plate (or Block) extrudes laterally to the west and is bounded by a set of conjugate strike-slip faults, referred to as the East and North Anatolia faults (EAF and NAF, respectively). By contrast, the northwestern Iranian Plateau does not show significant extrusion to the east [10]–[12]. Rather than large-scale features, a series of shorter discontinuous NW-SE-trending strike-slip faults (see Fig. 1)

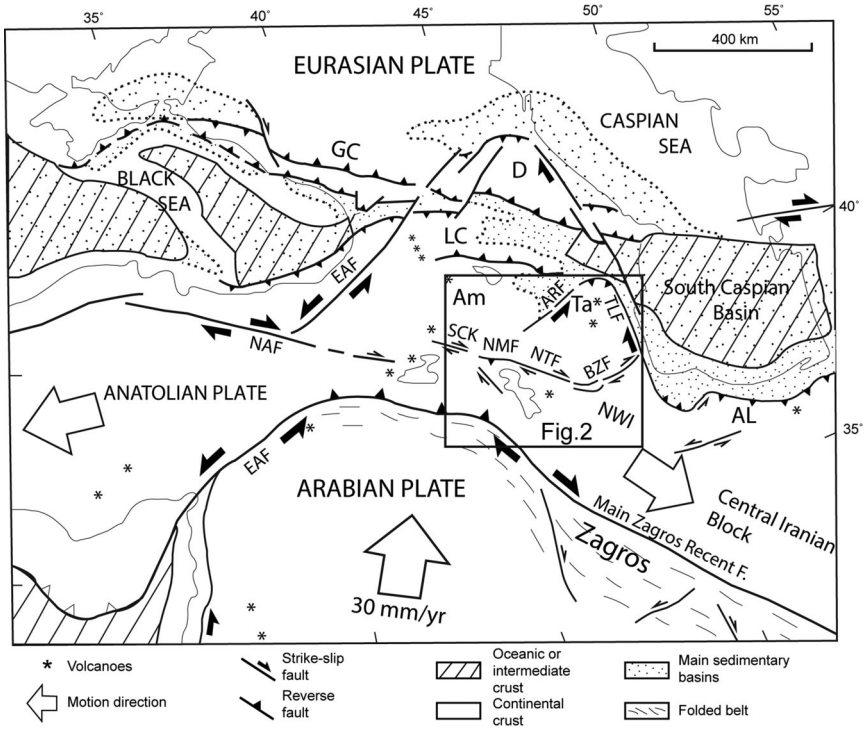

Fig. 1. (a) Tectonic framework of the Turkish-Iranian Plateau (modified from [20]). The major geologic structures are abbreviated as follows: AN: Anatolian block, AL: Alborz block, CI: Central Iranian block, GC: Greater Caucasus block, LU: Lut block, NWI: northwest Iranian block, and ZG: Zagros block.

replace those larger strike-slip faults in the northwestern Iranian Plateau [9], [13]. The North Mishu fault (NMF) and the North Tabriz fault (NTF) lie within a cryptic area of this orogen, where both the 2000-km-long NAF and the 600-km-long Zagros main recent fault disappear (see Fig. 1). How exactly the smaller scale features (e.g., NMF and NTF) relate to the larger scale strike-slip faults (e.g., the EAF and NAF) is unknown, but their relationship is key to understand how regional N-S shortening and E-W extension of the northwestern Iranian Plateau accommodates the Arabia-Eurasia plate collision [8], [14]–[19].

This study will try to explore the above scientific questions. We designed the analysis strategy to examine the following considerations.

The first objective is to obtain general knowledge of termination transformation. If a strike-slip fault transfers shear strain into vertical deformation at one of its termini, the original strike-slip fault and the newly activated thrust or normal fault will likely retain the original motion indicators in the transition zone. Therefore, the original attitudes of motion will not completely disappear and may appear as spatial changes in velocity vectors around the structure in question.

The second objective is to determine a proper method to constrain this slight variation. In this study, two geodetic measurements—GPS decomposition and the small baseline subset (SBAS) persistent scatterer interferometric synthetic aperture radar (PS-InSAR) method—are applied. GPS measurements can provide high-precision monitoring data, especially in the horizontal dimension. We plan to decompose the GPS horizontal velocity vectors into two directions: fault-parallel and fault-perpendicular slip rates. These two submotions will be coarsely used to represent the strike-slip and dip-slip rates along the target fault. However, GPS data have a coarse spatial resolution because of the low distribution density. The PS-InSAR is a complementary approach for this. It can provide a dense velocity field. However, the line-of-sight (LOS) rate is only a 1-D displacement velocity, unlike the three dimensions of GPS (e.g., eastward, northward, and vertical). However, the LOS mean rate is a composite velocity that is generally considered to be determined by both horizontal and vertical subcomponents.

Last but not least, why select the NTF-NMF fault system as the study area? GPS measurements have shown that the area around Yerevan city (capital of Armenia) moves northwest at a rate of ∼13 mm/yr (see Fig. 1) [21]. The ∼30-mm/yr trajectory of the Arabian Plate means that the regions in northwestern Iran must accommodate more than 50% of the N–S convergence of the plate (at least 17 mm/yr) [9]. Generally, in the absence of larger features, interseismic strain accumulation can be expressed on intracontinental faults. Alternatively, relatively small-scale strain features develop across large areas and are activated on a fairly infrequent basis. However, large-scale intracontinental faults have not been definitively documented in northwestern Iran. Instead, a set of small-scale dextral strike-slip faults most likely play a role in accommodating the relatively large proportion of interseismic deformation, although this has not been unaccounted for until now.

Following these strategies, we will apply the GPS decomposition and SBAS PS-InSAR technologies to constrain the possible termination dynamics along the NTF-NMF fault system.

II. Seismotectonic Setting

Earthquakes have posed a serious risk to Iranian cities and villages since ancient times [14]. Historical earthquakes in northwest Iran mainly occurred on three individual faults [see

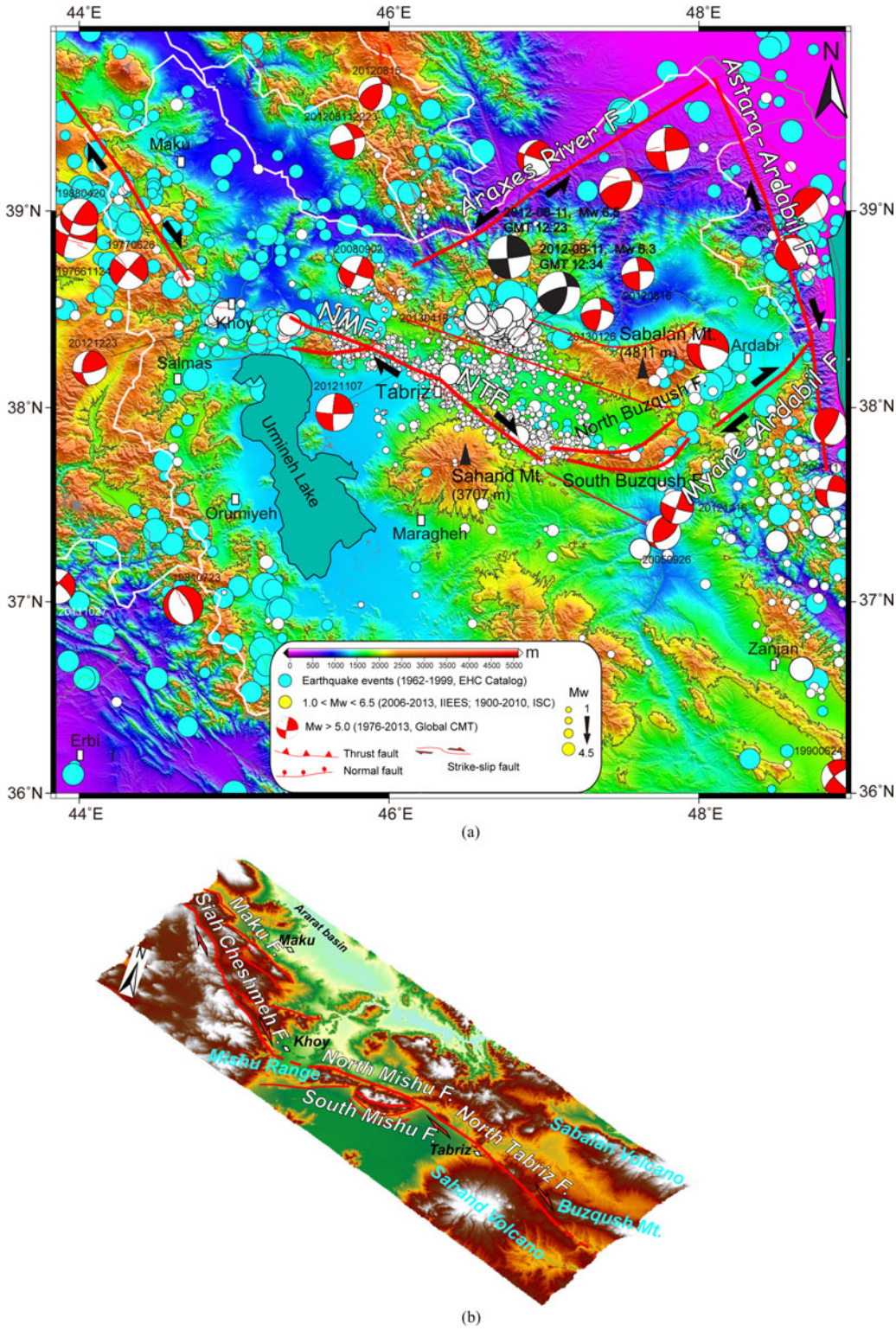

(a)

(b)

Fig. 2. (a) Seismic events affecting the northwestern Iranian Plateau. Teal circles represent $M < 3.0$ earthquake events listed in the Earthquake Hazard Centre (EHC) catalogue and a global catalogue of locations and magnitudes of instrumentally recorded earthquakes from 1900 to 2008 (one part of the global seismicity catalogue spans from 1964 to 1995 [24]; another catalogue spans from 1900 to 2008, including periodic updates with new arrival time data from 1999 to 2008, [25]). White circles represent earthquake events listed in the International Seismological Center catalogue (ISC, $1.0 < \text{Mw} < 6.5$, 2006–2013) and International Institute of Earthquake Engineering and Seismology database (IIEES, $1.0 < \text{Mw} < 6.5$, 1901–2010). Red and black beach balls show focal mechanism solutions for $M > 4.0$ earthquakes listed in the National Earthquake Information Center (NEIC, USGS, 1976–2013) and Global Centroid Moment Tensor catalogues (Global CMT, 1976–2013). The two black and white beach balls show focal mechanism solutions for the 11 August 2012 doublet earthquakes (Mw 6.5 and 6.3) that occurred in the Ahar region of northwest Iran. (b) 3-D representation of the SCK-NMF-NTF zone. The faults shown are related but are not continuous.

Fig. 2(a)]: the Siah Cheshmeh-Khoy fault (SCK) extending from Armenia to northwestern Iran, the NTF to the south, and the east-west-striking Mishu thrust fault zone (MTFZ) between the two aforementioned structures [see Fig. 2(b)] [14], [16], [19], [22], [23]. These structures are arranged in an S-shape in map view [see Fig. 2(b)].

Of the three faults, the NTF represents the most prominent linear structure in this region. The NTF is close to Tabriz, the largest city in northwestern Iran. The fault separates Eyn-Ali Mountain to the north from the Tabriz basin to the south. Historical records indicate that the NTF may have generated $M > 7.5$ earthquakes, but no $M > 7.0$ earthquakes have occurred in the past 235 years [14]. The most recent event on the NTF was the 11 August 2012 doublet earthquake (Mw 6.4 and 6.3; black and white beach balls in Fig. 2(a)). This pair of events caused over 300 deaths and left 3000 injured. The first earthquake of the doublet (Mw 6.4) occurred in the Ahar region at 12:23 UTC. The second event occurred 11 min later near the town of Ahar. Copley *et al.* [26] linked the events to splays of the NTF. The initial event occurred primarily as strike-slip displacement, whereas the second event exhibited both thrust and strike-slip motion [26].

Farther north, the NTF enters the Mishu Range, where it connects with the NMF. The NMF bounds the northern margin of the Mishu Range. It is a component of the MTFZ. The MTFZ consists of a series of nearly east-west-striking reverse faults [19], [27] (see Fig. 3). From west to east, these include the Tasuj, South Mishu (SMF), and Sufian faults (SUF). Earthquake activity has not occurred along the western segment of the NMF in historical times, whereas nearby faults appear to be more active. On 11 July 1807, a $M > 5.5$ earthquake occurred along the central part of the Tasuj fault (see Fig. 3). Fifty years later on 6 August 1857, another $M > 5.5$ event occurred along the eastern segment of the NMF [14].

A regional kinematic interpretation requires integration of the seismic history with an understanding of the complex structural relationships. Seismology offers many examples of spatiotemporal earthquake patterns that indicate stress transfer among neighbouring fault segments or systems. The NMF-NTF system is one such example. One $M \sim 7.4$ occurred along the central NTF in 1780 (see Fig. 3). Only six years later in 1786, the northern segment of the NTF ruptured again, along with the eastern segment of the NMF, together releasing a $M \sim 6.8$ earthquake [28] (see Fig. 3). While studies linking seismic events to changes in stress regime have emphasized the progressive nature of these events [29]–[31], tandem structures may rupture simultaneously. The 1957 (12/04) earthquake in Gobi-Altay, Mongolia, for example, included multiple simultaneous ruptures on both strike-slip and thrust fault systems [14].

III. GPS Decomposition

Conservation of stress transfer suggests that the decrease in right-lateral slip along the NTF should persist as some form of right-lateral slip along the NMF, independent of the thrusting motion of the latter. This study interprets recently published GPS data [21], [32]–[35] to derive estimates of the spatial variations in the strike- and dip-slip rates along the NMF, NTF, and their associated transition zone.

The GPS dataset includes horizontal velocity datasets from 14 permanent GPS stations operating from 1999 to 2009, as well as 14 temporary arrays. Because GPS vectors represent movement relative to a Eurasia-fixed reference frame and because the strike direction is quite different between the NTF and the NMF, we selected two local GPS stations as common reference points and transformed the data accordingly. Station TASJ was selected for the NMF estimates and station TABZ was chosen for the NTF estimates.

Certain zones are subject to limitations in data coverage due to the sparse distribution of GPS stations. Although the GPS measurements available in this region are sparse, some GPS sites are located very close to the faults. For example, the VLDN site is situated on the northern edge of the NMF and could be used to constrain the variation in the strike-slip rate of this fault. Furthermore, the SHAB and the AMND are located within or close to the transition zone of these two faults. We interpreted the fault-parallel slip rate as equivalent to the strike-slip rate for each fault. Although the fault-normal rate does not strictly equal the dip-slip rate, it does provide an estimate of the vertical deformation that is adequate for the purposes of this study.

A. Variation in Fault-Parallel and Fault-Normal Slip Rates Along/Across the NTF

Previous research has compared the interseismic slip rate of the NTF at different time scales. Vernant *et al.* [32], Reilinger *et al.* [21], Masson *et al.* [36], and Djamour *et al.* [34] used GPS monitoring to estimate a present-day strike-slip rate of 7–10 mm/yr along the fault. Hessami *et al.* [23] and Karakhanian *et al.* [19] used paleoseismic evidence to estimate a long-term slip rate of 2–4 mm/yr along the NTF. Rizza *et al.* [35] compared the PS-InSAR LOS mean rate (short-term) to estimates based on alluvial fan displacement (longer term). These workers found that both short- and long-term interseismic slip rates fell within a range of 6.5 to 7.3 mm/yr. Karimzadeh *et al.* [37] estimated a ~15.8-km locking depth from a mean small baseline InSAR slip rate of 8.7 ± 2.5 mm/yr. Su *et al.* [38] inverted the slip deficit distribution along the subsurface fault plane of the NTF using a combination of GPS and PS-InSAR data. These researchers speculated that the northern and central segments of the NTF are more active than the southern part of the fault. The northern and central segments have a locked depth of ~10 km, whereas the southern segment has an estimated locked depth of ~15–20 km. In summary, the strike-slip rate along the NTF ranges from approximately 6 to 10 mm/yr on decadal time scales.

The GPS velocities measured around the NTF are referenced to a permanent GPS station TABZ. These velocity vectors are transformed into a fault-parallel direction of N130°E and a fault-normal direction of N50°E [see Fig. 4(a)]. The fault-parallel slip rates indicate right-lateral strike-slip motion along the NTF relative to station TABZ. To the north, all fault-parallel velocity vectors trend northwest, indicating southeasterly motion of the

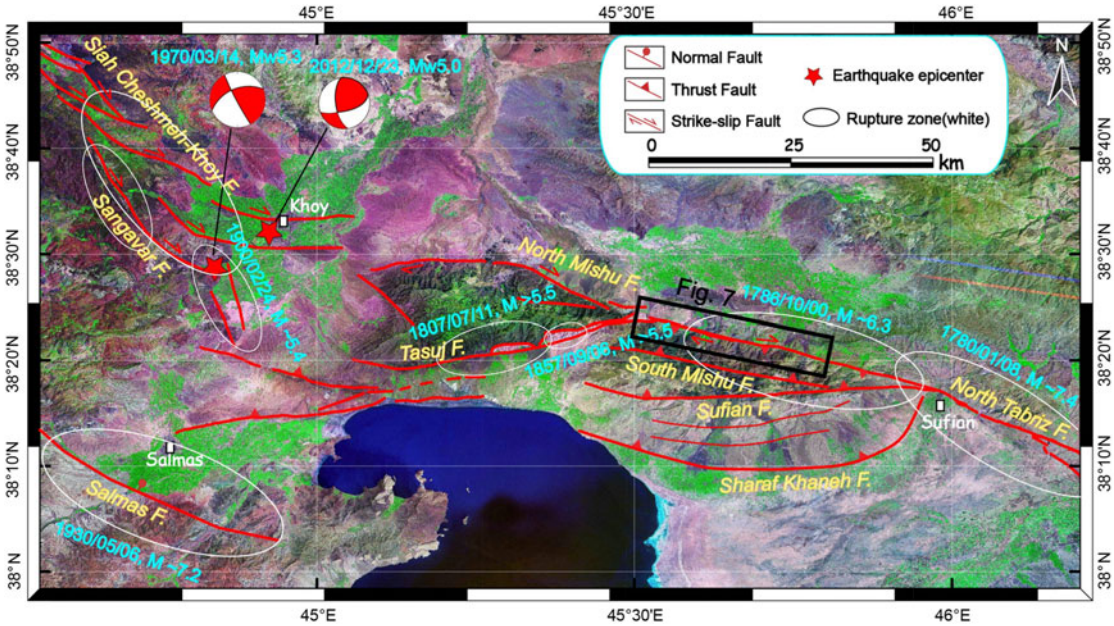

Fig. 3. Historical seismic activity along the MTFZ. Basemap from ETM+ Landsat images.

block to the south of the NTF [see Fig. 4(a)]. The strike-slip rates along transect BA exhibit smaller magnitudes relative to those measured along transect TA [see Fig. 4(b) and (c)]. The southeasterly lateral extrusion of the Talesh block appears to decrease from north to south [see Fig. 4(b)], although the local reference frame may contribute to this apparent effect. Almost all GPS velocities along the central segment of the NTF are less than 1.0 mm/yr, whereas the GPS stations in mountainous areas show greater magnitudes with respect to the TABZ site. This pattern may indicate interseismic activity in the Talesh block prior to the 12 August 2012 earthquake doublet, as well as prolonged accumulation of seismic strain.

Much more is known about the horizontal shearing movement than the vertical submotion along the NTF. Berberian [14], [28] speculated that the NTF may experience reverse deformation due to overthrusting of the northern block southward onto the southern block. The steep dip angle of the fault plane of the NTF makes it difficult to remotely distinguish between the hanging wall and footwall blocks. Furthermore, different NTF segments show differing vertical behavior. The fault-normal slip velocities of the northern block range from 0 to 1.0 mm/yr [see Fig. 4(a)] in a northeasterly or southwesterly direction. Pure strike-slip faults with steep fault planes (e.g., [39]) frequently show this type of behavior and geometry. The central part of the NTF further to the north shows a slight increase in fault-normal slip rates. With increasing proximity to the transition zone, the rates increase from 0.59 mm/yr near station TA04 to 0.71 mm/yr near station AMND [see Fig. 4(a)]. The ∼0.12-mm/yr shift occurs over a distance of ∼25 km. Although the fault-normal slip does not equal the dip-slip rate, the apparent increase of ∼0.005 mm/yr km provides a quantitative estimate the vertical shift.

The southern block of the NTF contains two main geological features: the Tabriz Basin and Sahand volcano. The maximum fault-normal slip rate of 1.32 mm/yr occurs along the south slope of Sahand volcano. Fault-parallel slip rates decrease linearly from south to north (defining northwestward motion as positive or "+"). A slip rate of 1.22 mm/yr was measured at station HSTD. At station BA04, the rate decreased to 1.15 mm/yr, then dropped further to 0.85 mm/yr at TA03, a station installed near the central segment of the NTF. The only GPS station in the MTFZ (SHAB) recorded a negative vector of −1.57 mm/yr [see Fig. 4(a)]. We inferred a region free of tectonic deformation between areas of positive and negative displacement. The shift in strike-slip rate from +0.85 mm/yr to −1.57 mm/yr over a distance of ∼30 km indicates subsurface structural features beneath the Tabriz Basin. The rate of change along this southern block of the NTF is ∼0.08 mm/yr km.

In summary, the transition from shear to compressive deformation along the southern block of the NTF appears to feature a more abrupt decrease in the fault-parallel slip rates (∼0.08 mm/yr km) than in the fault-normal rates (∼0.005 mm/yr km). The Talesh block, located to the north of the NTF, is experiencing large-scale extrusion to the southeast at a rate of 3 ± 0.5 mm/yr. This lateral motion appears to decrease from north to south.

B. Right-Lateral Strike-Slip Rate Along the NMF

The NMF consists of two fault branches (see Fig. 3): a western segment, extending from the village of Dizajbiz to the village of Baghlar [19], and an eastern segment, running along the northern foot of the Mishu Range. Because the GPS stations around the NTF and NMF measured only horizontal vectors [21], [34], the vertical motion of the fault zone remains uncertain. This study uses fault-normal slip rate data to estimate this parameter.

The Mishu Range has a total of four GPS stations [see Fig. 5(a)]. The data from these stations were processed according to a local reference frame provided by station TASJ. Given

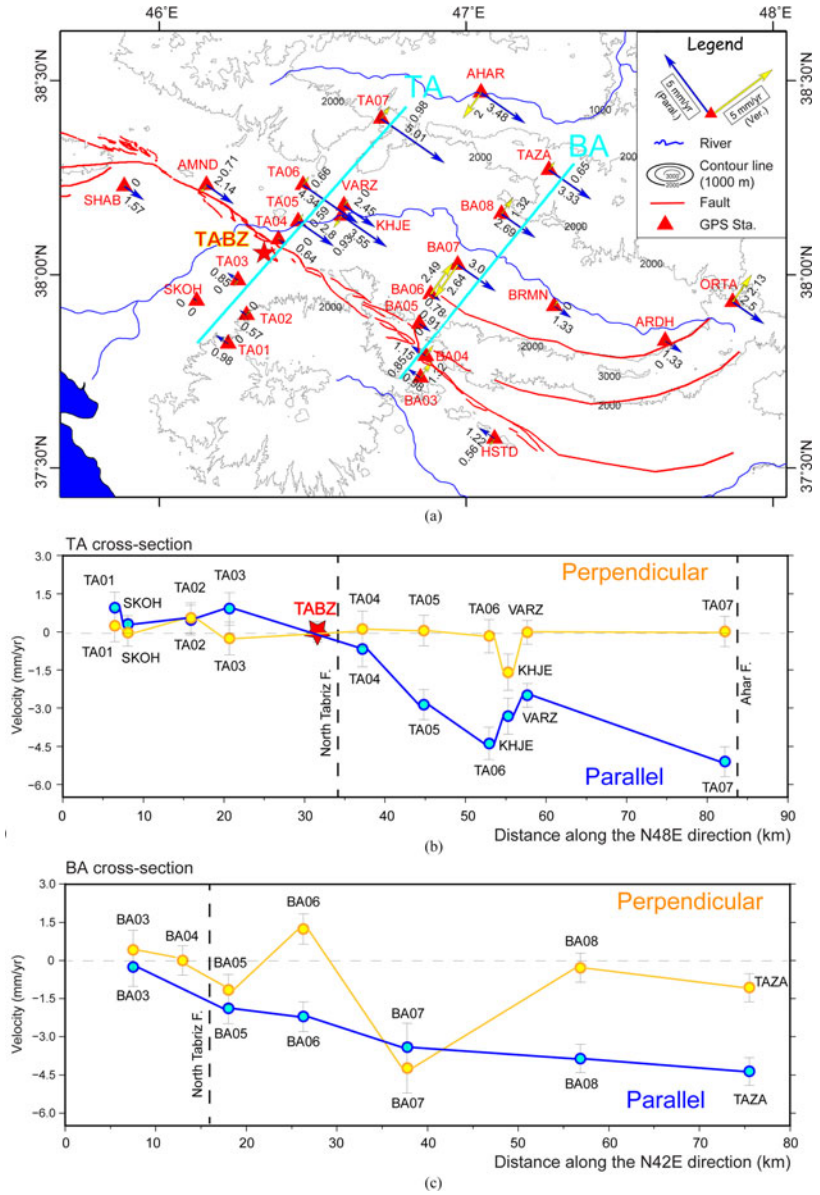

Fig. 4. (a) GPS velocity vectors are decomposed into fault-parallel (blue vectors) and fault-normal (yellow vectors) velocities for the NTF. The velocities are all calculated with respect to the permanent GPS station TABZ (red star). The two teal lines show the location of transects TA and BA as they traverse the NTF, striking N48°E and N42°E, respectively. (b) Fault-parallel (blue) and fault-normal (yellow) velocity estimates for transect TA across the central segment of the NTF. (c) Fault-parallel (blue line) and fault-normal (yellow line) velocity estimates for transect BA across the southern segment of the NTF.

the overall strike direction of the MTFZ, we decomposed all the GPS velocity vectors into the fault-parallel and fault-normal directions of N100°E and N20°E, respectively.

Relative to station TASJ, the fault-parallel slip rate near station VLDN was ∼2.62 mm/yr to the east [see Fig. 5(a)]. This indicates that the western NMF experiences right-lateral strike-slip motion, similar to the NTF. The fault-parallel slip rate also increases from north to south and displays the lowest values in the north [see Fig. 5(b)]. The fault-normal slip velocity vector at the GPS station VLDN (close to the NMF) indicates northward movement. These results suggest that the western segment of the NMF experiences northward thrusting. Furthermore, the region north of the NMF appears to move laterally to the east at an average fault-parallel rate of 5 mm/yr [JOLF, BSOF, and YKKZ in Fig. 5(a)].

The fault-normal slip rate in the Mishu Range regions increases from south to north, while the fault-parallel rate decreases in a northerly direction. In spite of the sparse GPS coverage, we conclude that the NMF is a transpressive fault, coupling right-lateral shear with northward thrusting. The block located to the north of the NMF may also move in an ESE direction, with movement also apparently decreasing from west to east. In this way, it resembles the NTF.

Speculation regarding the presence of right-lateral strike slip along the NMF could also be verified based on the seismic evidence. The 2012 Khoy basin earthquake provides additional evidence of remnant right-lateral slip along the NMF. A spoon-shaped pressure ridge appeared near the epicentre of the Mw 5.0 event, which occurred on 23 December 2012 in the Khoy basin (see Fig. 6). The pressure ridge strikes WNW-ESE, parallel to

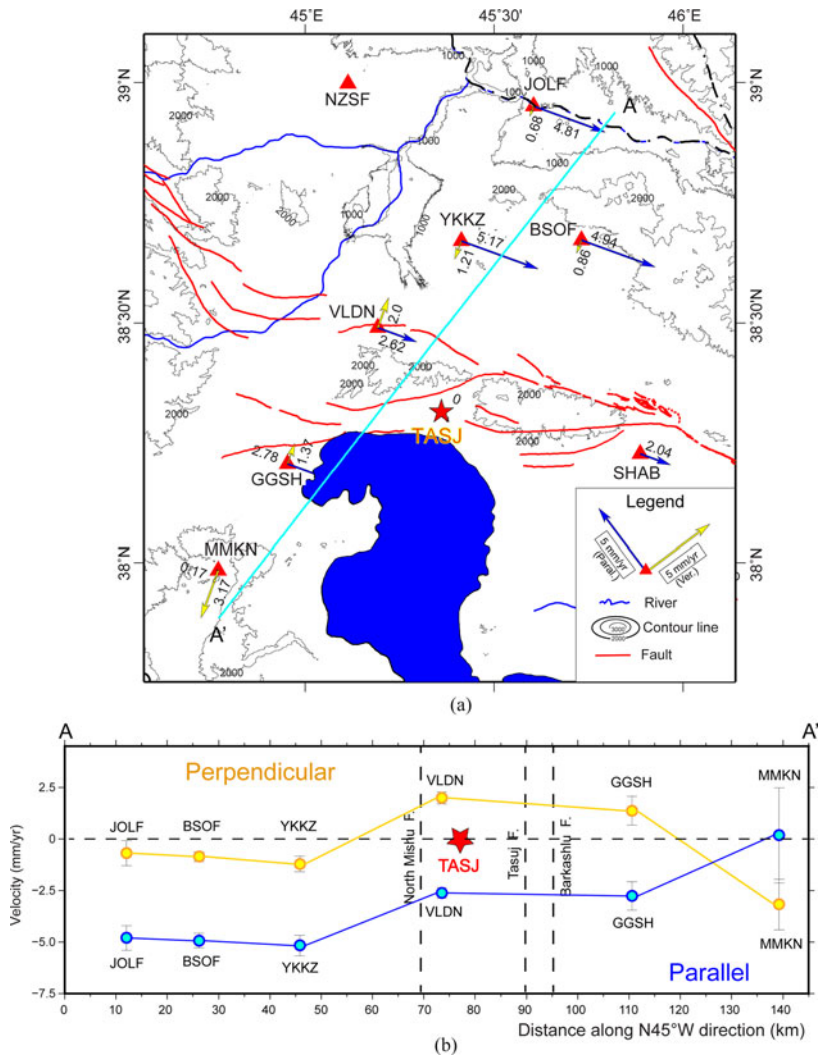

Fig. 5. (a) Map view of the GPS velocity vectors for the NMF. Velocities are decomposed into fault-parallel (blue) and fault-normal (yellow) slip rates along/across the NMF strike direction, as referenced to station TASJ. (b) Cross section of transect AA′ (teal line in panel (a) shows the subcomponents of fault-parallel (blue) and fault-normal (red) motion, as referenced to station TASJ).

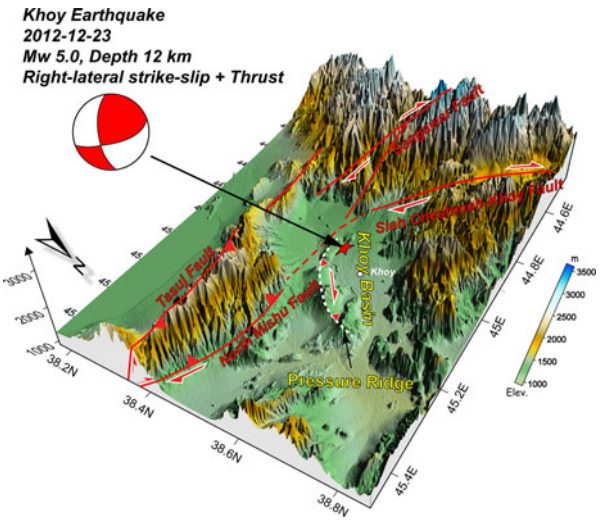

Fig. 6. Focal mechanism of the 23 December 2012 Mw 5.0 Khoy earthquake (based on the Global CMT earthquake catalogue). A pressure ridge that appeared in the Khoy basin may represent a transitional structure between the NTF and the NMF.

the NMF. The focal mechanism solution for the earthquake (red beach ball in the Fig. 6; data from the Global CMT catalogue) indicates both thrusting and right-lateral (WNW-ESE) strike-slip motion. Both the appearance of the pressure ridge and the focal mechanism solution indicate that right-lateral strike-slip motion does occur along the NMF.

C. Geomorphic Evidence for Right-Lateral Strike-Slip Along the NMF

The eastern segment seems to have been more active since the late Pleistocene, as evidenced by a series of river channels and valleys that have been apparently dislocated by the NMF (see Fig. 7). Maximal displacement occurs along a large river flowing from a source on the northern slope of Alamdar Mountain (3155 m). Flowing north, the river crosses the NMF at a point where its channel expresses ∼3 km of sudden dextral offset (to the east). The river channel then resumes northward flow. Farther to the north, the river also deposits a large volume of sediment onto the plain. The drainage channels of

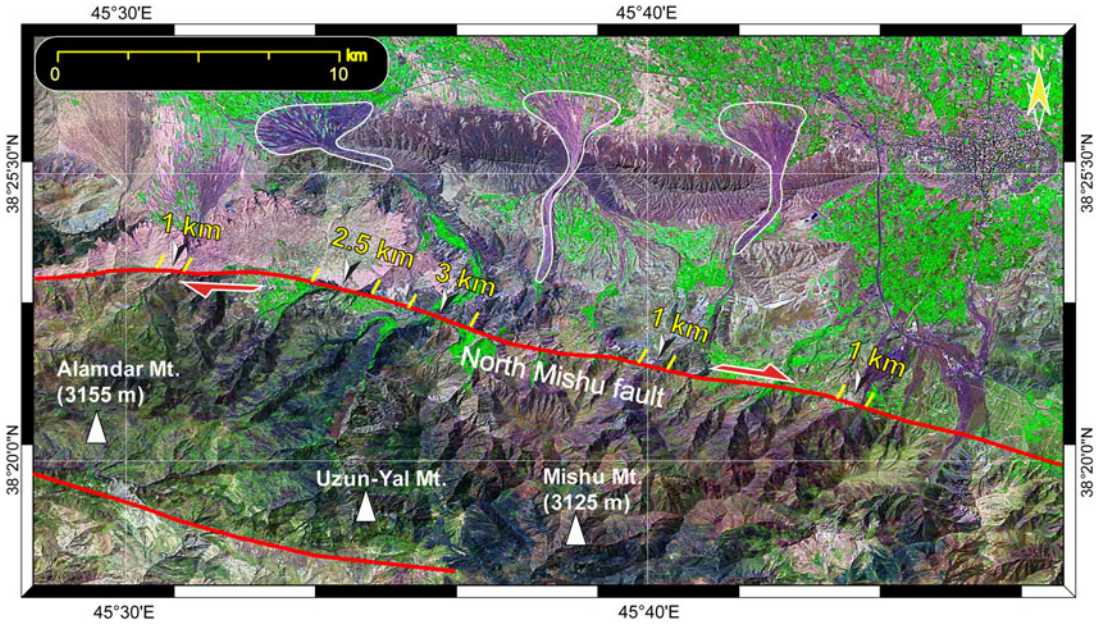

Fig. 7. Dextral offsets in river channels along the NMF. This figure uses the Landsat ETM+ image as the basemap.

adjacent rivers show similar right-lateral offset of approximately ∼1 km. The consistent offset of drainage channels in the vicinity of the NMF confirms our interpretation that significant right-lateral strike slip movement occurs along the NMF.

IV. Small Baseline PS-InSAR Monitoring

A. Methodology and Data

Studies of interseismic strain accumulation are crucial to our understanding of continental deformation, earthquake recurrence intervals, and seismic risk. In comparison with the relatively high slip rates on major plate boundary transform faults, such as the San Andreas system [40]–[42], the slip rates along intracontinental faults are always smaller in magnitude. The greater spatial extent and lower temporal consistency of these faults requires monitoring time frames to estimate the slip rates.

Space-borne InSAR techniques have the potential to dramatically improve the spatial density and continuity of surface displacement measurements, thereby complementing GPS and ground-based measurements. Examples of these techniques include conventional differential SAR interferometry using a stacking approach based on radar satellites [43] and persistent scatter SAR Interferometry (PS-InSAR, [44]–[46]). Although these two techniques have been used to accurately measure changes in the surface of the Earth due to earthquakes, landslides, regional tectonic activity, and groundwater extraction, their measurement density dramatically decreases in hilly areas. Phase variation due to decorrelation is often large enough to obscure the underlying signal in the absence of a dominant scatterer in radar pixels. This increases the difficulty of precisely mapping and interpreting creeping sections along several parts of the fault and measuring the ground velocity offset across the fault.

The SBAS interferometry technique is based on an appropriate combination of differential interferograms produced by data pairs characterized by a small orbital separation (baseline) in order to limit the spatial decorrelation phenomena [47]. The application of the singular value decomposition method allows us to easily "link" independent SAR acquisition datasets separated by large baselines, thus increasing the temporal sampling rate of the observations [47]. The availability of both spatial and temporal information in the processed data is used to identify and filter out atmospheric phase artefacts [48], [49].

In this study, we will apply the SBAS method to select relatively stable persistent scatters. The SBAS main processing chain is followed by [50]. The StaMPS software package (developed by Stanford University; [44], [51]) is used to process the radar images. StaMPS integrates ROI_PAC modules [52] from raw data with geocoded unwrapped interferograms and DORIS software (developed by the Delft Institute of Earth Observation and Space Systems of Delft University of Technology). Several new features of this software include the application of range-dependent spectral filtering to improve coherence in interferograms with long spatial baselines, the estimation and removal of digital elevation model (DEM) errors before unwrapping, a module that mitigates the effects of the atmospheric phase delay and removes residual orbit errors, and a module that constructs the phase change time series from the small baseline interferograms [44], [51]. We used a 3-D unwrapping method to unwrap the phase values of neighbouring persistent scatterers lying within half of a cycle. A standard Goldstein filter [53] was then used to reduce the decorrelation noise prior to phase unwrapping. The 3-arc (90-m resolution) Shuttle radar topography mission DEM dataset [54] was used to remove the topographic contribution.

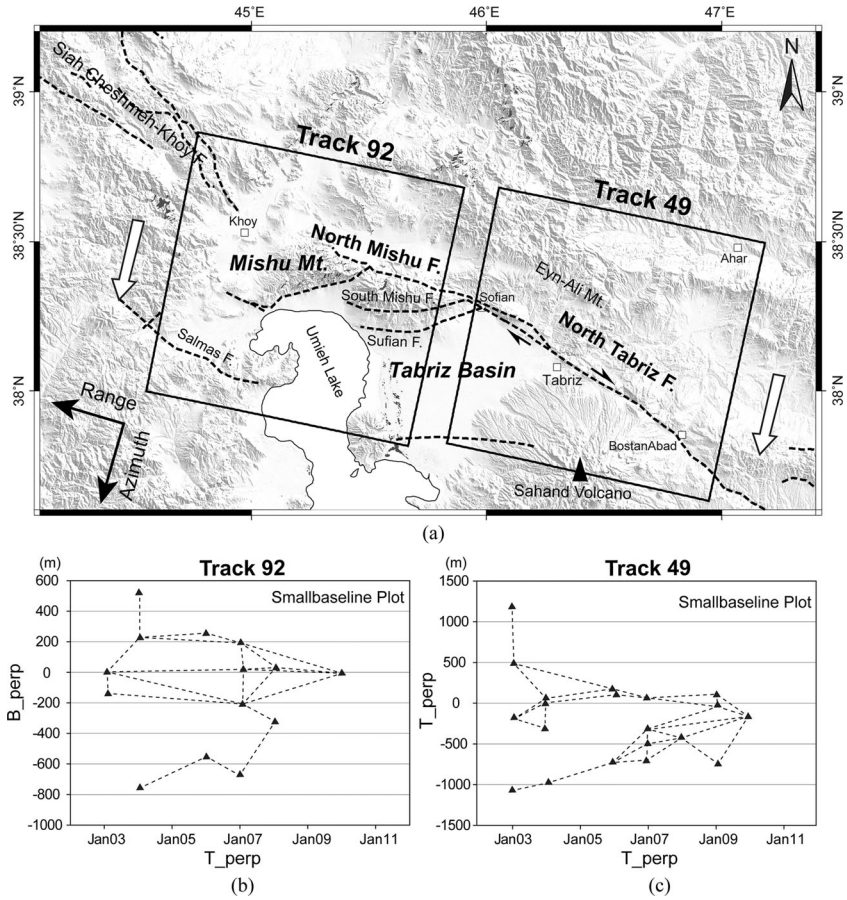

Fig. 8. (a) Radar satellite azimuth and coverage maps for Track 92 and Track 49. (b) Small baseline distribution for Track 92 used to investigate the MTFZ. (c) Small baseline distribution for Track 49 used to investigate the NTF.

We processed a total of 34 Envisat/ASAR descending-pass radar images from two frames [see Fig. 8(b) and (c)]. They were collected from May 2, 2003 to January 15, 2010. Of these, 14 raw radar images (Track 92) cover the Mishu fault zone, and 20 SLC format (Level 1.0) radar images cover the NTF (Track 49) [see Fig. 8(a)]. The Envisat/ASAR satellite sensor captures the relatively short-wavelength C-wave band ($\sim$2.8 cm). This permits millimetre-scale estimates of surface displacement over large areas. Shorter wavelength detection constrains more subtle deformational signals, especially under interseismic conditions. Lacking dense vegetation or significant urban development, the desert and mountainous terrain of the northwestern Iranian Plateau offers an excellent locality for monitoring these types of subtle features.

B. Interseismic Velocity Field

We selected a total of 75 008 and 67 500 PS pixels for the NTF and NMF, respectively. The density of PS pixels exceeded 15 points per km^2. We used warm tones (e.g., red and yellow) and cold tones (e.g., blue) to represent relative ground movement toward and away the satellite.

The northern block of the NMF seems to exhibit westward extrusion, as shown by the warm tone of the region in Fig. 9. This motion tendency resembles that occurring to the north of the NTF. This motion could induce the NMF to express right-lateral strike-slip motion in addition to thrusting. Together with the NTF, these two dextral faults comprise a relatively large fault system along the leading edge of the convergence zone between the Arabian and Eurasian plates. The NMF-NTF system may, therefore, act as a plate boundary accommodating lateral extrusion of the northwestern Iranian Plateau as it moves toward the Central Iranian block. The magnitude of this extrusion, however, is smaller than that occurring along the EAF and NAF to the west.

A linear NE-SW-striking feature referred to as F1 appears along the southern wall of the NTF. F1 extends from the northwestern slope of Sahand volcano to the northeast, where it joins with the NTF to form a conjugate fault system. This NE-SW-striking fault has not been previously reported; only a series of small-scale and discontinuous NW-SE right-lateral faults distributed in the northwest Iranian Plateau has been reported [9]. Our SBAS results may provide additional evidence concerning the discussion of how right-lateral strike-slip faults alone accommodate lateral extrusion of the northwestern Iranian Plateau. At least one conjugate fault system exists south of the NTF, although some of its faults are buried beneath the Tabriz basin. Unlike the NAF and EAF to the west, the conjugate fault system of the northwestern Iranian Plateau accommodates the N–S compression resulting from the convergence of the Arabian and Eurasian plate, rather than lateral extrusion of the entire block.

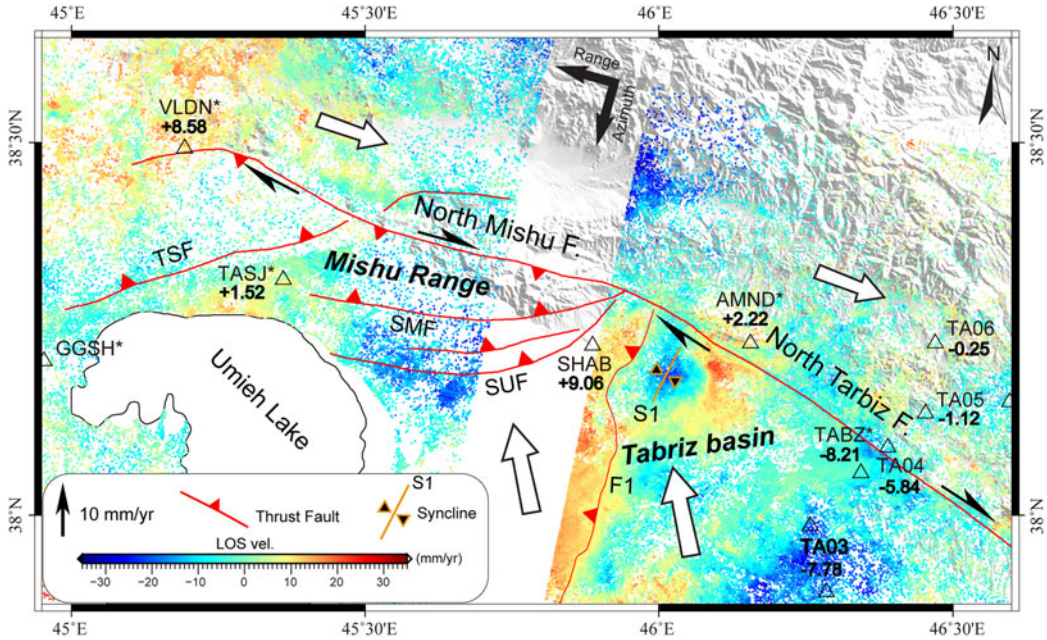

Fig. 9. LOS velocity fields for the MTFZ and the NTF. Vertical velocities (Vu) were calculated using circular search areas centred on each GPS station, along with east and north GPS velocity components (Ve and Vn, respectively) from the GPS data. Asterisks (∗) represent permanent GPS stations. The transects A1–A2 and B1–B2 run parallel to the strike of the NTF as shown in the Fig. 11. TSF: Tasuj fault, SMF: South Mishu fault, and SUF: Sufian fault.

We also noticed that F1 separates a zone of uplift (warm colours) from a zone of subsidence (cool colours) to the east. Thrust activity may contribute to the uplift of the former area and create an adjacent down-dropped zone. We, therefore, interpret the area colored with cool tones as a developing syncline. Although the axial region of the syncline is apparently moving away from the point of reference, the overall area is experiencing shortening. Reverse faults, including the SUF, SMF, and F1, appear around the terminations of the NTF. These thrust faults may absorb the northwestward movement of the southern wall of the NTF. We further speculate that the Tabriz basin is a compressional basin situated in front of the continuous northwestward motion of the Arabian plate.

C. *Vertical Displacement Rate*

Most previous studies of northwestern Iran have evaluated the Quaternary strike-slip rates along faults [21], [32]–[35]. The stress transferred along a strike-slip fault always transitions from horizontal shearing to compressive uplift or extensional release at the terminations. Thus, the termination behaviors are always represented by a change in vertical velocity. However, the lack of precision in vertical GPS estimates probably prevents a focus on this type of stress transfer research.

Although the SBAS method only provides a 1-D movement estimate in the satellite-and-ground system, the mean rate of displacement along the LOS direction exactly represents a composite velocity vector that is determined by both horizontal (Ve and Vn) and vertical (Vu) subcomponents [55]. Thus, if three of the four variables—Ve, Vn, Vu, and LOS—are known, the remaining variable can be calculated based on the spatial geometric relationships shown in Fig. 10. Equation (1) shows how

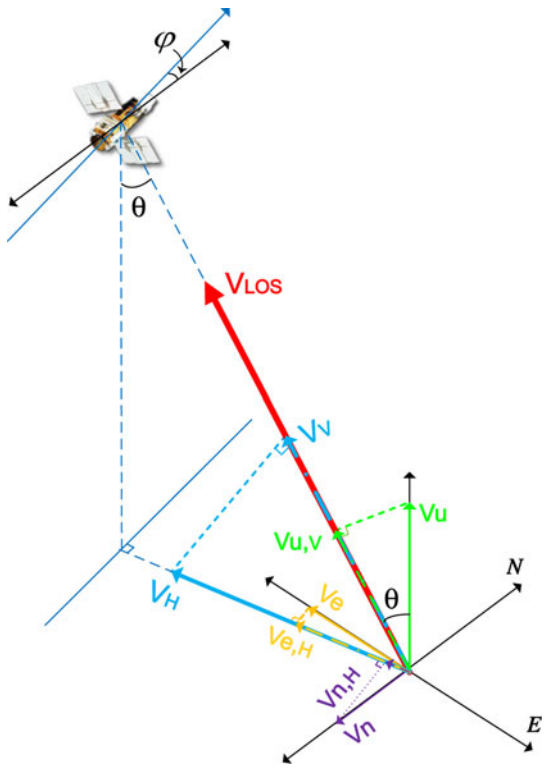

Fig. 10. Decomposition of the displacement velocity vector along the LOS (modified from [57]). Here, φ is the azimuth of the satellite flight path (positive clockwise from north), and θ is the incidence angle at the reflection point. V_{LOS} is the LOS displacement rate; V_e is the easting displacement velocity; V_n is the northing displacement velocity; V_u is the vertical displacement rate; $V_{u,V}$ is the vertical displacement rate projected into the LOS direction, V_V; $V_{e,H}$ and $V_{n,H}$ are the projected velocities from the eastward and northward movement contributions, V_H; V_{LOS} is the total contribution from the horizontal V_H and vertical V_V in the LOS direction.

TABLE I
REVERSE CALCULATION OF VERTICAL VELOCITY WITH 1-SIGMA UNCERTAINTIES FOR EACH GPS STATION*

Site	Vu (mm/yr)	Vu, los (mm/yr)	$\mathrm{LOS}_{\mathrm{near}}$ (mm/yr)	Δ (mm/yr)	Dis. (m)
AMND	2.22	2.04	2.74	0.7	600
SHAB	9.06	9.34	7.77	1.57	1000
TA03	−7.78	−7.17	−18.32	11.15	500
TA04	−5.84	−5.38	−6.85	1.47	600
TA05	−1.12	−1.03	−4.48	3.45	230
TA06	−0.25	−0.23	−1.62	0.39	280
TABZ	−8.21	−7.56	−8.87	1.31	2700
TASJ	1.52	1.4	2.8	1.4	180
VLDN	3.82	3.52	7.71	4.19	120

The GPS results are relative to a Eurasia-fixed reference frame
*: GPS data collected from 1999 to 2009 [34]. Stations AMND, TABZ, TASJ, and VLDN include continuous GPS measurements [34]. Stations SHAB, TA03, TA04, TA05, and TA06 were operated during discrete survey periods. The SHAB station operated for 48 h at least three times from 2000 to 2008 [34]. The other four stations within the TA profile operated for at least 48 h during each survey [35]. Stations also operated four times during the fall of 2004–2008 except for TA04, which operated in the fall of 2005, 2006, and 2008; [35]. The PS dataset, thus, spans a period from 2003 to 2010. The time intervals for the GPS and PS datasets overlap for seven years. Vu: vertical velocity; Vu, los: conversion result from vertical velocity into the LOS direction; $\mathrm{LOS}_{\mathrm{near}}$: the PS pixel LOS displacement rate closest to each GPS site; Δ: difference between the LOS mean rate at the nearest PS pixel and the conversion result from vertical velocity for each GPS site; and Dis.: the distance between each GPS site and the closest PS pixel.

to compute the vertical velocity rate:

$$\mathrm{Vu} = d_{\mathrm{los}} - (Ve \bullet \cos\varphi + Vn \bullet \sin\varphi) \bullet \tan\theta \qquad (1)$$

This calculation must accommodate different monitoring reference frames for the GPS data (calculated relative to the Eurasia-fixed frame) and the SBAS PSI result (relative movement within the ground-satellite system). The two frames of reference for radar images do not overlap, precluding selection of a common reference point [56]. However, we can unify their reference frames onto the Eurasia-fixed frame. The LOS mean rate can also be converted into this frame along the LOS direction. Following the formulas in [55] and [56], we calculate the total contribution of the horizontal subcomponents in the LOS direction (see Fig. 10), $V_H = V_{e,H} + V_{n,H}$. Then, multiplying the vertical velocity by the cosine of the incidence angle, we obtain the total vertical contribution in the LOS direction, $V_V = V_{u,v} = Vu * \cos$. As d_{los} is determined by the horizontal eastward and northward subcomponents and the vertical submotion, the sum of V_H and V_V is equal to the LOS rate (see Fig. 10), $d_{\mathrm{los}} = V_H + V_V$. Generally, a PS pixel is not always present at the point location of each GPS site. Thus, we search for the PS point closest to the GPS station. The mean LOS displacement rate is used to represent the d_{los} achieved from PS-InSAR (see Table I).

The Mishu Range hosts only three GPS stations, VLDN, TASJ, and SHAB. The vertical velocities from these stations each indicate uplift, which is consistent with prominent thrust movement in the area. Almost all the vertical velocities along the central segment of the NTF (e.g., transect TA) appear to move away from the satellite. Tabriz city, for example, is moving away from the current satellite position at a rate of −8.79 mm/yr. We interpret this motion as land subsidence potentially caused by intensive groundwater pumping in Tabriz city. The GPS station TA03 is situated on the northwest slope of the Sahand volcano. It is apparently moving away from the satellite reference point in the LOS direction. This motion may be related to Sahand magmatic activity at depth, e.g., growth or deflation of lava domes. Stations TA05 and TA06 located on Eyn-Ali Mountain do not indicate significant vertical deformation. Eyn-Ali Mountain appears to experience primarily lateral extrusion, rather than shortening or extension.

We also projected all the vertical velocities into the LOS direction, $V_{u,\mathrm{los}}$. Then, we compared them with the LOS mean rate at the nearest persistent scatter point around each GPS site (the nearest PS pixel should be the only PS pixel within the searching distance; see Table I). With the exception of the TA03 site, which has a large difference (11.15 mm/yr), the differences are small, with a range of $<$5.0 mm/yr.

V. DISCUSSION

A. Termination Mechanism Approaching the Termini of Strike-Slip Faults

The spatial distribution of strain transfer between faults was first examined by Anderson [58]. Chinnery [59] later described deformation in a uniform elastic half-space as having a characteristic distribution of vertical deformation that accompanies slip. Large intracontinental strike-slip faults, however, are seldom linear or continuous, and deformation along these structures is usually distributed over wide areas, e.g., [11], [60]. Permanent strain fields appear around faults, resulting in complex geometries due to continued slip [61]. Consequently, these strike-slip faults cannot easily interface with other major structures in the same way that, for example, transform faults connect ridge or trench segments [62].

Two types of transform patterns generally appear at the termini of strike-slip faults [3]. One pattern involves the simple disappearance of the fault into undeformed regions. For example, extensive east-west-striking faults in northeastern Iran disappear as they enter tectonically stable areas of Afghanistan, e.g., [63]. The relatively flat and featureless Gobi Desert shows no signs of the faults that enter the region from the eastern Gobi-Altay of Mongolia [64]. Another common accommodation pattern involves the transfer of stress from strike-slip faults to more dispersed deformational structures. At both ends of a strike-slip fault, areal strain contraction can produce restraining bends or uplift. In eastern and northeastern Tibet, for example, faults transition into distributed thrusts in the Longmen Shan, e.g., [65], and Qilian Shan, e.g., [66].

The transitional dynamics operating in the NTF-NMF fault zone are, thus, fairly unique but can still serve as a point of reference for other complex structural areas. For the sake of comparison, we calculated rate change per distance estimates to quantify the horizontal-to-vertical transfer at the strike-slip fault terminus. For the NTF-NMF fault system, the fault-parallel slip

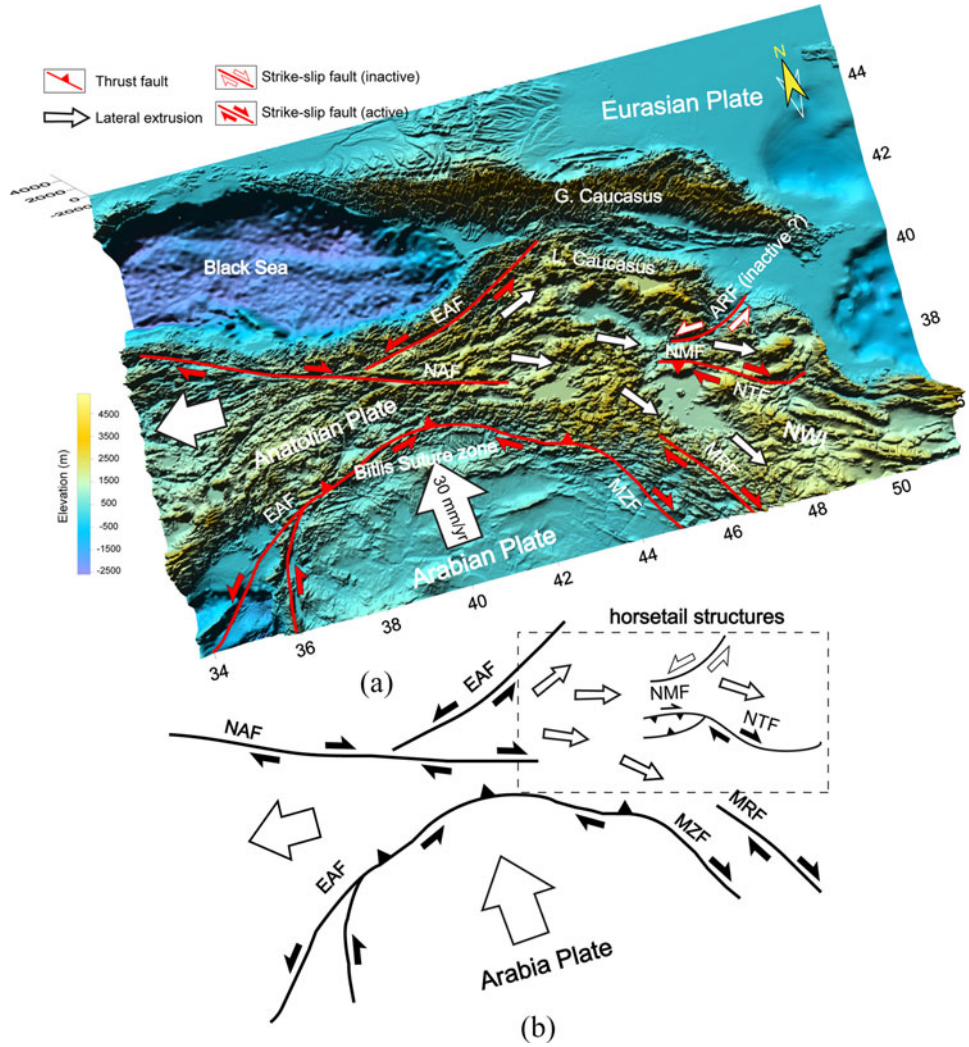

Fig. 11. Geographic map (a) and tectonic framework (b) of the Turkish-Iranian Plateau. The EAF and NAF form a conjugate strike-slip system that accommodates lateral extrusion of the Anatolian Plate. The smaller sized unfilled arrows represent small-scale extrusion of the northwestern Iranian Plateau. EAF: East Anatolia fault, NAF: North Anatolia fault, G. Caucasus: Greater Caucasus, L. Caucasus: Lesser Caucasus, MZF: Main Zagros fault, MRF: Main Recent fault, NMF: North Mishu fault, NTF: North Tabriz fault, and NWI: Northwestern Iranian Plateau.

rate for the NTF decreases at a rate of 0.08 mm/yr km as shear is transferred to the NMF to the north. Fault-normal slip rates meanwhile increase at a rate of 0.005 mm/yr km. The vertical motion rate increases at a rate of 0.38 (from TABZ to SHAB) and 0.36 mm/yr km (from TA04 to AMND). In summary, as the strike-slip fault converts shearing into thrusting, the fault-parallel slip decreases by an order of magnitude more than the amount of change observed in the fault-normal slip.

B. Small-Scale Extrusion Accommodated By Horsetail Structures

Conjugate fault systems play an important role in accommodating plate or subcontinent movement away from a collision zone [67]. In the case of the Tibetan Plateau, lateral displacement along a series of large-scale strike-slip faults accommodates the northward collision of India into Eurasia. These structures include the left-lateral Altyn Tagh fault in the north, the left-lateral East Kunlun fault in central regions, the right-lateral Jiali fault in the south, and the left-lateral Xianshuihe–Xiaojiang and right-lateral Red River–Ailao Shan faults in the southeast, as well as numerous other smaller scale faults. These strike-slip features trend primarily NE-SW and NW-SE, forming a rhombohedral-shaped block (in map view). Left- or right-lateral shearing along these structures accommodates coeval E–W elongation and N–S contraction within the Tibetan Plateau and in surrounding regions, e.g., [68]. These boundary faults, thus, guide regional tectonic blocks, such as the Tarim Basin, laterally away from the collision zone [5], [59]. The Chuan-Dian block, for example, is moving toward Southeast Asia, a geologically unique region bordering the Tibetan Plateau along its southeastern margin, e.g., [69].

The 2000-km-long left-lateral NAF and right-lateral EAF form the boundary between Eurasia and Anatolia, two previously contiguous blocks [see Fig. 11(a)]. These two large-scale conjugate fault systems accommodated westward extrusion of the Anatolian Plate as a whole after Miocene ocean closure along the Bitlis suture [70]. Although it represents a major

continent-continent collision zone, northwestern Iran (to the east) does not clearly exhibit far-field lateral extrusion accommodated by conjugate strike-slip faults [9], [13]. The only feature active for a duration long enough to perform such a function is the left-lateral NE-SW-striking Araxas River fault [ARF; Fig. 11(a)]. Previous research, however, indicates that the ARF is no longer active [19]. Therefore, the northwestern Iranian block lacks an adequate structural mechanism for accommodating egress from the collision zone.

In tectonic escape systems, discrete pieces of continental lithosphere not only move away from loci of convergence in a coherent fashion, they also experience internal deformation and develop a large degree of bulk strain along their edges. The NMF-NTF fault zone exhibits these traits. This study presents novel geodetic evidence that both the NMF and NTF express right-lateral shear motion. Thrusting along the NMF most likely inherits stress transferred from the right-lateral strike-slip motion along the NTF. These two small-scale and apparently independent faults may have interacted under a previous kinematic regime.

As the Arabian Plate continues to move northwestward, numerous small-scale and discontinuous right-lateral strike-slip faults have developed throughout the northwestern Iranian Plateau. These structures, including the NMF-NTF, the MRF, and the MZF [see Fig. 11(b)] are inferred from the surface expressions of fault segments via methods that may not accurately estimate cumulative fault length. Along with the large-scale EAF farther to the northwest, scattered transfer structures form a horsetail pattern along the eastern terminus of the NAF. As such, they accommodate approximate N–S convergence and E–W extension associated with the Arabian Plate collision. These dispersed intracontinental structures allow small-scale aseismic deformation and local rotation. Transitional structures also convert shear stress into compression expressed as folds or fault bends.

VI. Conclusion

This study analyzed the regional velocity vectors from permanent and temporary GPS arrays to estimate changes in the fault-parallel and fault-normal slip rates of the transition zone between the NTF and NMF, a critical area of far-field stress transfer accommodating the Arabia-Eurasia Plate collision. In northwestern Iran, the fault-parallel slip rate of the NTF decreases at a rate of 0.08 mm/yr km as shear stress is transferred to the NMF to the north. The fault-normal slip rates meanwhile increase at a rate of 0.005 mm/yr km. Accordingly, the vertical rate increases at a rate of 0.38 mm/yr km. A subcomponent of right-lateral strike-slip remains evident along the NMF. The results, thus, generally show that when a strike-slip fault transfers shear onto a thrust fault, the fault-parallel slip rate will decrease by an order of magnitude more than the change in the rate of fault-normal slip. The northern block of the NMF-NTF fault zone is moving laterally to the east, but slows toward the southern terminus of the NTF. This produces a series of hidden NE-SW-striking thrust faults and a syncline developing in and around the Tabriz basin. Thereafter, the Tabriz basin is a compressional basin between mountains. Although the northwestern Iranian Plateau does not include obvious large-scale extrusive structures, smaller distributed horsetail structures, including relatively short and discontinuous strike-slip faults, appear to accommodate the far-field effects of N–S shortening and E–W extension resulting from the collision of the Arabian and Eurasian plates.

Acknowledgment

The authors would like to thank the European Space Agency for providing Envisat/ASAR radar images (Project CAT-1-8094) and the Global Land Cover Facility for providing the Landsat ETM+ remote sensing images. They would also like to thank three reviewers' constructive suggestions.

References

[1] A. A. Barka and K. Kadinsky-Cade, "Strike-slip fault geometry in Turkey and its influence on earthquake activity," *Tectonics*, vol. 7, no. 3, pp. 663–684, Jun. 1988.

[2] R. Freund, "Kinematics of transform and transcurrent faults," *Tectonophysics*, vol. 21, nos. 1/2, pp. 93–134, Jan. 1974.

[3] A. G. Sylvester, "Strike-slip faults," *Geol. Soc. Amer. Bull.*, vol. 100, no. 11, pp. 1666–1703, Nov. 1988.

[4] P. Z. Zhang, P. Molnar, and X. Xu, "Late quaternary and present-day rates of slip along the Altyn Tagh Fault, northern margin of the Tibetan Plateau," *Tectonics*, vol. 26, no. 5, Oct. 2007, Art. no. TC5010.

[5] P. Zhang *et al.*, "Continuous deformation of the Tibetan Plateau from global positioning system data," *Geology*, vol. 32, no. 9, pp. 809–812, Sep. 2004.

[6] P. Tapponnier *et al.*, "Active thrusting and folding in the Qilian Shan, and decoupling between upper crust and mantle in northeastern Tibet," *Earth Planet. Sci. Lett.*, vol. 97, nos. 3/4, pp. 382–403, Mar. 1990.

[7] E. Wang *et al.*, "Late Cenozoic Xianshuihe-Xiaojiang, Red River, and Dali fault systems of southwestern Sichuan and central Yunnan, China," *Geol. Soc. Amer. Spec. Paper*, vol. 327, pp. 1–108, 1998.

[8] A. Copley and J. Jackson, "Active tectonics of the Turkish-Iranian Plateau," *Tectonics*, vol. 25, no. 6, Dec. 2006.

[9] J. Jackson and N. Ambraseys, "Convergence between Eurasia and Arabia in eastern Turkey and the Caucasus," in *Historical and Prehistorical Earthquakes in the Caucasus*, D. Giardini and S. Balassanian, Eds. Dordrecht, The Netherlands: Kluwer, 1997, pp. 79–90.

[10] M. B. Allen, E. J.-P. Blanc, R. Walker, J. Jackson, M. Talebian, and M. R. Ghassemi, "Contrasting styles of convergence in the Arabia-Eurasia collision: Why escape tectonics does not occur in Iran," *Geol. Soc. Amer. Spec. Paper*, vol. 409, pp. 579–589, Jan. 2006.

[11] D. McKenzie, "Active tectonics of the Mediterranean region," *Geophys. J. Int.*, vol. 30, no. 2, pp. 109–185, Jun. 1972.

[12] T. Taymaz, J. Jackson, and D. McKenzie, "Active tectonics of the north and central Aegean Sea," *Geophys. J. Int.*, vol. 106, no. 2, pp. 433–490, Mar. 1991.

[13] J. Jackson, "Partitioning of strike-slip and convergent motion between Eurasia and Arabia in eastern Turkey and the Caucasus," *J. Geophys. Res.*, vol. 97, no. B9, pp. 12471–12479, Aug. 1992.

[14] M. Berberian, "Seismic sources of the Transcaucasian historical earthquakes," in *Historical and Prehistorical Earthquakes in the Caucasus*, D. Giardini and S. Balassanian, Eds. Dordrecht, The Netherlands: Kluwer, 1997, pp. 233–311.

[15] M. Berberian and G. C. P. King, "Towards a paleogeography and tectonic evolution of Iran," *Can. J. Earth Sci.*, vol. 18, no. 2, pp. 210–265, Feb. 1981.

[16] M. Berberian and R. S. Yeats, "Patterns of historical earthquake rupture in the Iranian Plateau," *Soc. Amer.*, vol. 89, no. 1, pp. 120–139, Feb. 1999.

[17] A. Cisternas and H. Philip, "Seismotectonics of the Mediterranean region and the Caucasus," in *Historical and Prehistorical Earthquakes in the Caucasus*, vol. 28, D. Giardini, S. Balassanian, Eds. Dordrecht, The Netherlands: Kluwer, 1997, pp. 39–77.

[18] A. Karakhanian, R. Djrbashian, V. Trifonov, H. Philip, S. Arakelian, and A. Avagian, "Holocene-historical volcanism and active faults as natural risk factors for Armenia and adjacent countries," *J. Volcanol. Geotherm. Res.*, vol. 113, nos. 1/2, pp. 319–344, Mar. 2002.

[19] A. S. Karakhanian *et al.*, "Active faulting and natural hazards in Armenia, eastern Turkey and northwestern Iran," *Tectonophysics*, vol. 380, nos. 3/4, pp. 189–219, Mar. 2004.

[20] H. Philip, A. Cisternas, A. Gvishiani, and A. Gorshkov, "The Caucasus: An actual example of the initial stages of continental collision," *Tectonophysics*, vol. 161, nos. 1/2, pp. 1–21, Apr. 1989.

[21] R. Reilinger *et al.*, "GPS constraints on continental deformation in the Africa-Arabia-Eurasia continental collision zone and implications for the dynamics of plate interactions," *J. Geophys. Res.*, vol. 111, no. B5, May 2006.

[22] N. N. Ambraseys, C. P. Melville, and R. D. Adams, *The Seismicity of Egypt, Arabia and the Red Sea: A Historical Review*. Cambridge, MA, USA: Cambridge Univ. Press, 2005.

[23] K. Hessami *et al.*, "Paleoearthquakes and slip rates of the North Tabriz fault, NW Iran: Preliminary results," *Ann. Geophys.*, vol. 46, no. 5, pp. 903–915, Oct. 2003.

[24] E. R. Engdahl, R. van der Hilst, and R. Buland, "Global teleseismic earthquake relocation with improved travel times and procedures for depth determination," *Bull. Seismol. Soc. Amer.*, vol. 88, no. 3, pp. 722–743, Jun. 1998.

[25] E. R. Engdahl and A. Villaseñor, "Global seismicity: 1900–1999," in *International Handbook of Earthquake and Engineering Seismology, Part A*, vol. 81, W. H. K. Lee, H. Kanamori, P. C. Jennings, and C. Kisslinger, Eds. San Diego, CA, USA: Academic, 2002, ch. 41, pp. 665–690.

[26] A. Copley *et al.*, "The 2012 August 11 Ahar earthquakes: Consequences for tectonics and earthquake hazard in the Turkish-Iranian Plateau," *Geophys. J. Int.*, vol. 196, no. 1, pp. 15–21, Oct. 2013.

[27] M. Berberian, "Earthquake faulting and bedding thrust associated with the Tabas-e-Golshan (Iran) earthquake of September 16, 1978," *Soc., Amer.*, vol. 69, no. 6, pp. 1861–1887, Dec. 1979.

[28] M. Berberian, "On the evidence of the youngest activity of the North Tabriz fault and the seismicity of Tabriz city," *Geol. Surv. Iran Rep.*, vol. 39, pp. 397–418, Jan. 1976.

[29] R. S. Stein and M. Lisowski, "The 1979 homestead valley earthquake sequence, California: Control of aftershocks and postseismic deformation," *J. Geophys. Res.*, vol. 88, no. B8, pp. 6477–6490, Aug. 1983.

[30] S. Stein, J. F. Engeln, D. A. Wiens, K. Fujita, and R. C. Speed, "Subduction seismicity and tectonics in the Lesser Antilles arc," *J. Geophys. Res.*, vol. 87, no. B10, pp. 8642–8664, Oct. 1982.

[31] R. S. Stein, G. C. King, and J. Lin, "Change in failure stress on the southern San Andreas fault system caused by the 1992 magnitude = 7.4 Landers earthquake," *Science*, vol. 258, no. 5086, pp. 1328–1332, Nov. 1992.

[32] P. Vernant *et al.*, "Present-day crustal deformation and plate kinematics in the Middle East constrained by GPS measurements in Iran and northern Oman," *Geophys. J. Int.*, vol. 157, no. 1, pp. 381–398, Dec. 2004.

[33] F. Masson *et al.*, "Large-scale velocity field and strain tensor in Iran inferred from GPS measurements: New insight for the present-day deformation pattern within NE Iran," *Geophys. J. Int.*, vol. 170, no. 1, pp. 436–440, Apr. 2007.

[34] Y. Djamour, P. Vernant, H. R. Nankali, and F. Tavakoli, "NW Iran-eastern Turkey present-day kinematics: Results from the Iranian permanent GPS network," *Earth Planet. Sci. Lett.*, vol. 307, nos. 1/2, pp. 27–34, Jul. 2011.

[35] M. Rizza *et al.*, "Morphotectonic and geodetic evidence for a constant slip-rate over the last 45 kyr along the Tabriz fault (Iran)," *Geophys. J. Int.*, vol. 193, no. 3, pp. 1083–1094, Jan. 2013.

[36] F. Masson *et al.*, "Extension in NW Iran driven by the motion of the South Caspian basin," *Earth Planet. Sci. Lett.*, vol. 252, nos. 1/2, pp. 180–188, Nov. 2006.

[37] S. Karimzadeh *et al.*, "Interseismic strain accumulation across the North Tabriz Fault (NW Iran) deduced from InSAR time series," *J. Geodyn.*, vol. 66, pp. 53–58. 2013.

[38] Z. Su, J.-C. Hu, M. Talebian, and S. Karimzadeh, "A joint analysis of GPS and PS-InSAR to infer the fault segmentation and interseismic strain accumulation for the North Tabriz fault, NW Iran," in *Proc. EGU General Assembly Conference Abstracts*, May 2014, vol. 16, p. 6754.

[39] A. S. Moradi, D. Hatzfeld, and M. Tatar, "Microseismicity and seismotectonics of the north Tabriz fault (Iran)," *Tectonophysics*, vol. 506, nos. 1–4, pp. 22–30, Jun. 2011.

[40] I. A. Johanson and R. Bürgmann, "Creep and quakes on the northern transition zone of the San Andreas fault from GPS and InSAR data," *Geophys. Res. Lett.*, vol. 32, no. 14, Jul. 2005.

[41] R. Bürgmann, G. Hilley, A. Ferretti, and F. Novali, "Resolving vertical tectonics in the San Francisco Bay area from permanent scatterer InSAR and GPS analysis," *Geology*, vol. 34, no. 3, pp. 221–224, Mar. 2006.

[42] Y. Fialko, "Interseismic strain accumulation and the earthquake potential on the southern San Andreas fault system," *Nature*, vol. 441, no. 7096, pp. 968–971, Jun. 2006.

[43] R. Bürgmann *et al.*, "Earthquake potential along the northern Hayward fault, California," *Science*, vol. 289, no. 5482, pp. 1178–1182, 2000.

[44] A. Hooper, D. Bekaert, K. Spaans, and M. Arıkan, "Recent advances in SAR interferometry time series analysis for measuring crustal deformation," *Tectonophysics*, vols. 514–517, pp. 1–13, Jan. 2012.

[45] A. Ferretti, F. Ferrucci, C. Prati, and F. Rocca, "SAR analysis of building collapse by means of the permanent scatterers technique," in *Proc. IEEE Int. Geosci. Remote Sens. Symp.*, Honolulu, HI, USA, 2000, pp. 3219–3221.

[46] A. Ferretti, C. Prati, and F. Rocca, "Permanent scatterers in SAR interferometry," *IEEE Trans. Geosci. Remote Sens.*, vol. 39, no. 1, pp. 8–20, Jan. 2001.

[47] P. Berardino, G. Fornaro, R. Lanari, and E. Sansosti, "A new algorithm for surface deformation monitoring based on small baseline differential SAR interferograms," *IEEE Trans. Geosci. Remote Sens.*, vol. 40, no. 11, pp. 2375–2383, Nov. 2002.

[48] J. Biggs, T. Wright, Z. Lu, and B. Parsons, "Multi-interferogram method for measuring interseismic deformation: Denali Fault, Alaska," *Geophys. J. Int.*, vol. 170, no. 3, pp. 1165–1179, 2007.

[49] R. Jolivet, R. Grandin, C. Lasserre, M. P. Doin, and G. Peltzer, "Systematic InSAR tropospheric phase delay corrections from global meteorological reanalysis data," *Geophys. Res. Lett.*, vol. 38, Sep. 2011, Art. no. L17311.

[50] M.-P. Doin *et al.*, "Presentation of the small baseline NSBAS processing chain on a case example: The Etna deformation monitoring from 2003 to 2010 using Envisat data," presented at the Eur. Space Agency Symp. "Fringe", Frascati, Italy, Sep. 2011.

[51] A. Hooper, P. Segall, and H. Zebker, "Persistent scatterer interferometric synthetic aperture radar for crustal deformation analysis, with application to Volcán Alcedo, Galápagos," *J. Geophys. Res.*, vol. 112, no. B7, Jul. 2007.

[52] P. A. Rosen, S. Hensley, G. Peltzer, and M. Simons, "Updated repeat orbit interferometry package released," *Eos Trans. Amer. Geophys. Union*, vol. 85, no. 5, pp. 47–47, Feb. 2004.

[53] R. M. Goldstein and C. L. Werner, "Radar interferogram filtering for geophysical applications," *Geophys. Res. Lett.*, vol. 25, no. 21, pp. 4035–4038, Nov. 1998.

[54] T. G. Farr *et al.*, "The shuttle radar topography mission," *Rev. Geophys.*, vol. 45, no. 2, May 2007, Art. no. RG2004.

[55] Y. Fialko, M. Simons, and D. Agnew, "The complete (3-D) surface displacement field in the epicentral area of the 1999 M W 7.1 Hector Mine Earthquake, California, from space geodetic observations," *Geophys. Res. Lett.*, vol. 28, no. 16, pp. 3063–3066, Aug. 2001.

[56] M. Huang *et al.*, "Active deformation of Tainan tableland of southwestern Taiwan based on geodetic measurements and SAR interferometry," *Tectonophysics*, vol. 466, nos. 3/4, pp. 322–334, Mar. 2009.

[57] A. H. Ng, L. Ge, K. Zhang, and X. Li, "Estimating horizontal and vertical movements due to underground mining using ALOS PALSAR," *Eng. Geol.*, vols. 143/144, pp. 18–27, Aug. 2012.

[58] E. M. Anderson, *The Dynamics of Faulting and Dyke Fomation With Application to Britain*, 2nd ed. Edinburgh, U.K.: Oliver & Boyd, 1951.

[59] M. Chinnery, "The deformation of the ground around surface faults," *Bull. Seismol. Soc. Amer.*, vol. 51, no. 3, pp. 355–372, Jul. 1961.

[60] P. Molnar and P. Tapponnier, "Cenozoic tectonics of Asia: Effects of a continental collision: Features of recent continental tectonics in Asia can be interpreted as results of the India-Eurasia collision," *Science*, vol. 189, no. 4201, pp. 419–426, Aug. 1975.

[61] R. Bilham and G. King, "The morphology of strike-slip faults: Examples from the San Andreas fault, California," *J. Geophys. Res.*, vol. 94, no. B8, pp. 10204–10216, Aug. 1989.

[62] A. Bayasgalan and J. A. Jackson, "A re-assessment of the faulting in the 1967 Mogod earthquakes in Mongolia," *Geophys. J. Int.*, vol. 138, no. 3, pp. 784–800, May 1999.

[63] J. Jackson and D. McKenzie, "Active tectonics of the Alpine-Himalayan belt between western Turkey and Pakistan," *Geophys. J. Int.*, vol. 77, no. 1, pp. 185–264, Apr. 1984.

[64] W. D. Cunningham, B. F. Windley, L. A. Owen, T. Barry, D. Dorjnamjaa, and J. Badamgarav, "Geometry and style of partitioned deformation within a late Cenozoic transpressional zone in the eastern Gobi Altai Mountains, Mongolia," *Tectonophysics*, vol. 277, no. 4, pp. 285–306, Aug. 1997.

[65] B. C. Burchfiel, C. Zhiliang, L. Yupinc, and L. H. Royden, "Tectonics of the Longmen Shan and adjacent regions, central China," *Int. Geol. Rev.*, vol. 37, no. 8, pp. 661–735, Jul. 1995.

[66] B. Meyer *et al.*, "Crustal thickening in Gansu-Qinghai, lithospheric mantle subduction, and oblique, strike-slip controlled growth of the Tibet plateau," *Geophys. J. Int.*, vol. 135, no. 1, pp. 1–47, Feb. 1998.
[67] P. Tapponnier, G. Peltzer, and R. Armijo, *On the Mechanics of the Collision between India and Asia*. London, U.K.: Geological Society, 1986.
[68] M. Taylor, A. Yin, F. J. Ryerson, P. Kapp, and L. Ding, "Conjugate strike-slip faulting along the Bangong-Nujiang suture zone accommodates coeval east-west extension and north-south shortening in the interior of the Tibetan Plateau," *Tectonics*, vol. 22, no. 4, Aug. 2003.
[69] Z. Su, E. Wang, K. P. Furlong, X. Shi, G. Wang, and C. Fan, "Young, active conjugate strike–slip deformation in West Sichuan: Evidence for the stress–strain pattern of the southeastern Tibetan Plateau," *Int. Geol. Rev.*, vol. 54, no. 9, pp. 991–1012, Jul. 2012.
[70] A. M. C. Şengör, N. Görür, and F. Şaroğlu, "Strike-slip faulting and related basin formation in zones of tectonic escape: Turkey as a case study," in *Strike-Slip Deformation, Basin Formation, and Sedimentation*, vol. 37, K. T. Biddle and N. Christie-Blick, Eds. Tulsa, OK, USA: Society of Economic Paleontologists and Mineralogists, Dec. 1985, pp. 227–264.

Zhe Su was born in Xinji, He-Bei, China. He received the Ph.D. degree in structural geology with a certificate of commendation from the Institute of Geology and Geophysics, Chinese Academy of Sciences, China, in 2011.

From 2012 to 2014, he worked as a Postdoctoral Research Fellow in the Geodesy and Remote Sensing Laboratory, Department of Geosciences, National Taiwan University, Taiwan. He is currently working as an Associate Research Fellow with the Institute of Crustal Dynamics, China Earthquake Administration, Haidian, Beijing, China. His research interests include SAR interferometry, GPS measuring for inter-, co-, and postseismic deformation in the Tibetan Plateau, Greater and Lesser Caucasus, and Turkish-Iranian Plateau.

Er-Chie Wang was born in Shanghai, China. He received the Ph.D. degree in philosophy with a certificate of commendation from Massachusetts Institute of Technology, Cambridge, MA, USA, in 1994.

From 1994 to 1997, he worked as a Postdoctoral Research Fellow in Max's Corporation, USA. He is currently working with the Institute of Geology and Geophysics, Chinese Academy of Sciences, Chaoyang, Beijing, China. His research interest includes structural geology in the Tibetan plateau.

Jyr-Ching Hu was born in Taipei, Taiwan. He received the Ph.D. degree in structural geology from the Univerité Pierre et Marie Curie (University Paris 6), France, in 1995.

He is currently a Full Professor in the Department of Geosciences, National Taiwan University, Taipei, Taiwan. His research interests include SAR interferometry, geodetic measurements and numerical simulations for crustal deformation, earthquake cycle, and monitoring of landslide and land subsidence in Taiwan, Vietnam, Tibetan Plateau, Greater and Lesser Caucasus, and Turkish-Iranian Plateau.

Morteza Talebian was born in Neyshabour, NE Iran. He received the Ph.D. degree in active tectonics and seismology from the University of Cambridge, Cambridge, U.K., in 2003.

Along with his education, he has been a Member of Seismotectonic Department, Geological Survey of Iran, since 1990, and then the Head of department, from 1996 to 2007. His job was to perform filed investigation and study of active faults with especial attention to recent earthquakes and their relations to active tectonic of Iranian Plateau. In 2007, he moved to Research Institute for Earth Sciences and starts his academic career with involving in teaching and research at the same time. In 2009, he was appointed as the Director of RIES and managed several internal and international projects. His current research interest includes morphotectonic study of active faults and earthquake hazard assessment.

Sadra Karimzadeh was born in Tabriz, East-Azerbaijan, Iran. He received the Ph.D. degree in engineering with a certificate of commendation from Kanazawa University, Kanazawa, Japan, in 2015.

He is currently working as a Postdoctoral Research Fellow in the Department of GIS and Remote Sensing, University of Tabriz, Tabriz, Iran. His research interests include SAR interferometry, radar imagery for earthquake damage assessment, GIS applications for disaster management, and more recently seismic site characterizations based on GIS and remote sensing technologies. He also serves as a Reviewer for most of the international journals in remote sensing and earthquake engineering.